Article

Exploding and weeping ceramics

https://doi.org/10.1038/s41586-021-03975-5

Received: 22 September 2020

Accepted: 31 August 2021

Published online: 17 November 2021

Check for updates

Hanlin Gu[1,5]✉, Jascha Rohmer[2,5]✉, Justin Jetter[2]✉, Andriy Lotnyk[3,4]✉, Lorenz Kienle[2]✉, Eckhard Quandt[2]✉ & Richard D. James[1]✉

The systematic tuning of crystal lattice parameters to achieve improved kinematic compatibility between different phases is a broadly effective strategy for improving the reversibility, and lowering the hysteresis, of solid–solid phase transformations[1–11]. (Kinematic compatibility refers to the fitting together of the phases.) Here we present an apparently paradoxical example in which tuning to near perfect kinematic compatibility results in an unusually high degree of irreversibility. Specifically, when cooling the kinematically compatible ceramic $(Zr/Hf)O_2(YNb)O_4$ through its tetragonal-to-monoclinic phase transformation, the polycrystal slowly and steadily falls apart at its grain boundaries (a process we term weeping) or even explosively disintegrates. If instead we tune the lattice parameters to satisfy a stronger 'equidistance' condition (which additionally takes into account sample shape), the resulting material exhibits reversible behaviour with low hysteresis. These results show that a diversity of behaviours—from reversible at one extreme to explosive at the other—is possible in a chemically homogeneous ceramic system by manipulating conditions of compatibility in unexpected ways. These concepts could prove critical in the current search for a shape-memory oxide ceramic[9–12].

A general strategy for improving the reversibility of solid–solid phase transformations in crystals, as measured by the width of the hysteresis loop[6], by the migration of the transformation temperature[1] or by transformational fatigue[2,8,12], is to improve the geometric compatibility of the phases. A typical situation for non-perfect compatibility, notable in martensitic materials but also present in oxides, is to observe a stressed transition layer between the transforming phases. This transition layer separates twinned martensite from austenite. A widely accepted idea for reversible transformations is that there is an equipartition between the elastic energy of the stressed transition layer and the total interfacial energy on the twin boundaries[13–15]. Improving geometric compatibility refers to strategies that decrease the elastic energy in these transition layers via tuning of the lattice parameters. The term supercompatibility refers to the complete elimination of these stressed transition layers.

As an example of behaviour possible under conditions of supercompatibility, we put forward $Ti_{54.7}Ni_{30.7}Cu_{12.3}Co_{2.3}$, which, in well-prepared macroscopic samples, undergoes 10 million cycles of full stress-induced transformation (in tension) under applied stresses of ~400 MPa for each cycle, with no detectable change of the stress–strain curve[2]. The general strategy has been applied in metallic systems and recently with success in oxide systems[9–11].

During a systematic search for reversible phase transformations and shape memory in ceramics based on improving geometric compatibility, we encountered the unexpected behaviour described in the Abstract. The exploding samples evidently accumulated significant stress, despite a significant body of work cited above linking perfect compatibility and reversibility.

Other examples with different explanations advanced by the authors include an abrupt 'jumping' during reverse transformation in $Cu_{12.2}Al_{4.3}Fe_{6.6}Mn_{76.9}$ (ref. [16]) and related effects in molecular crystals[17–19]. Many of these transformations have unusually low symmetry (for example, monoclinic to monoclinic), so that, with only a single variant, reversible twinning as a mechanism for stress relief is not a possibility. A classic example of extreme explosive behaviour is Prince Rupert's drop (see refs. [20,21]) obtained by quenching a glass drop; in this case, an externally imposed nucleation event is typically required. Our explanation for the diverse behaviours in the $(Zr/Hf)O_2(YNb)O_4$ system is quantitative and could be applied to other systems.

The system $(Zr/Hf)O_2(YNb)O_4$ shows the same phase transformations as bulk ZrO_2, which exhibits a first-order monoclinic-to-tetragonal phase transformation at 1,170 °C and a tetragonal-to-cubic transformation at 2,370 °C. This high-temperature transformation plays no role in our studies. Our samples were polycrystalline with an average grain size of about 1.5 μm and equiaxed grains (Extended Data Fig. 1). The samples are chemically homogeneous as demonstrated by transmission electron microscopy (Extended Data Figs. 2–6). There, X-ray spectroscopy and analysis in both direct and reciprocal space indicate that short-range ordering or clustering of the metal atoms is not significant, either inside grains or at grain boundaries (see ref. [22]). Our X-ray measurements in the system $(Zr_yHf_{1-y}O_2)_{0.775}(Y_{0.5}Nb_{0.5}O_2)_{0.225}$ are all consistent with a tetragonal-to-monoclinic phase transformation on cooling (Extended Data Figs. 7 and 8).

As now recognized in an increasing number of systems, the $(Zr/Hf)O_2(YNb)O_4$ system has multiple lattice correspondences (Fig. 1),

[1]Department of Aerospace Engineering and Mechanics, University of Minnesota, Minneapolis, MN, USA. [2]Institute for Materials Science, Faculty of Engineering, Kiel University, Kiel, Germany. [3]Leibniz Institute of Surface Engineering (IOM), Leipzig, Germany. [4]Present address: Laboratory of Infrared Materials and Devices, The Research Institute of Advanced Technologies, Ningbo University, Ningbo, China. [5]These authors contributed equally: Hanlin Gu, Jascha Rohmer. ✉e-mail: guxxx369@umn.edu; jaro@tf.uni-kiel.de; juje@tf.uni-kiel.de; andriy.lotnyk@iom-leipzig.de; lk@tf.uni-kiel.de; eq@tf.uni-kiel.de; james@umn.edu

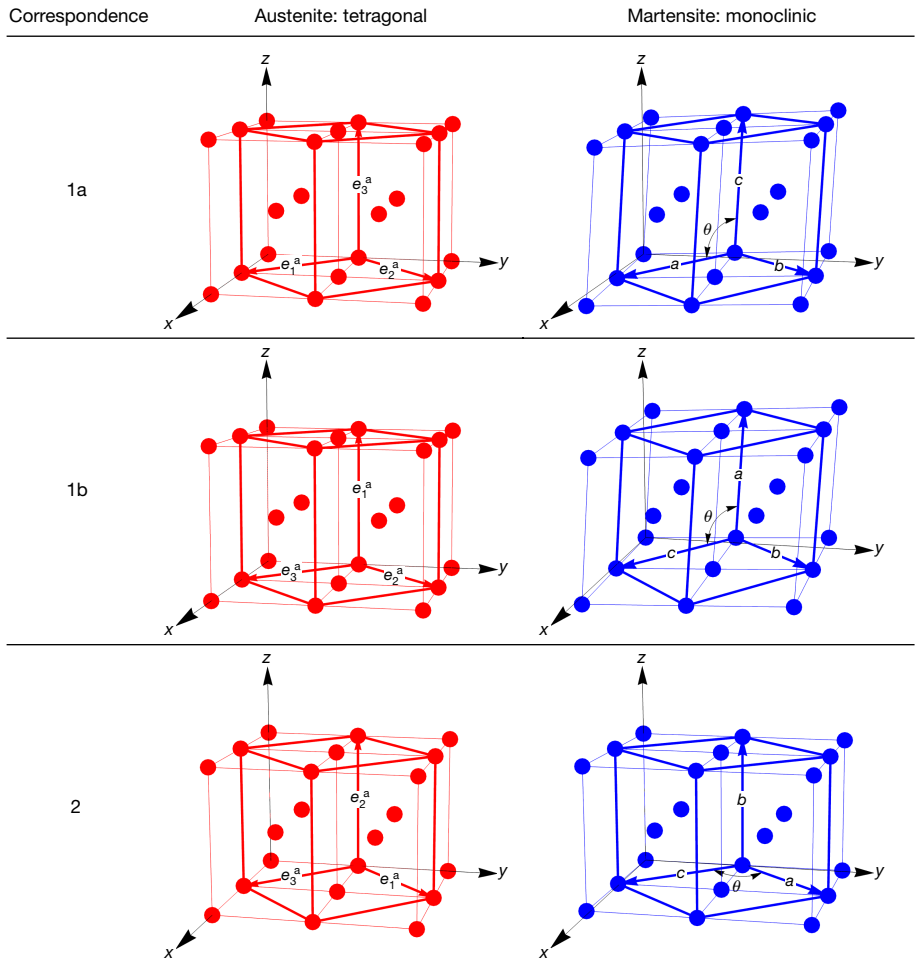

Correspondence	Lattice correspondence (tetragonal→monoclinic)	$U^{tet-mono}$	Eigenvalue
1a	$[1\bar{1}0]\rightarrow[100]$, $[110]\rightarrow[010]$, $[001]\rightarrow[001]$	$\begin{bmatrix} 1.01026 & 0.0027374 & -0.053784 \\ 0.0027374 & 1.01026 & 0.053784 \\ -0.053784 & 0.053784 & 1.02012 \end{bmatrix}$	$\lambda_1 = 0.93750$ $\lambda_2 = \mathbf{1.0130}$ $\lambda_3 = 1.09014$
1b	$[001]\rightarrow[100]$, $[110]\rightarrow[010]$, $[1\bar{1}0]\rightarrow[001]$	$\begin{bmatrix} 1.02976 & -0.016767 & -0.053758 \\ -0.016767 & 1.02976 & 0.053758 \\ -0.053758 & 0.053758 & 0.98209 \end{bmatrix}$	$\lambda_1 = 0.93174$ $\lambda_2 = \mathbf{1.0130}$ $\lambda_3 = 1.09688$
2	$[110]\rightarrow[100]$, $[001]\rightarrow[010]$, $[1\bar{1}0]\rightarrow[001]$ $([1\bar{1}0]\rightarrow[100]$, $[001]\rightarrow[010]$, $[110]\rightarrow[001])$	$\begin{bmatrix} 0.94993 & -0.019505 & 0 \\ -0.019505 & 1.10398 & 0 \\ 0 & 0 & 0.98757 \end{bmatrix}$	$\lambda_1 = -0.94750$ $\lambda_2 = \mathbf{0.98757}$ $\lambda_3 = 1.10641$

Fig. 1 | Lattice correspondences and transformation stretch matrices. The three correspondences observed in the $(Zr/Hf)O_2(YNb)O_4$ system showing conventional unit cells. The stretch matrices $U^{tet-mono}$ define the linear transformations that map the tetragonal cell (red) to the monoclinic cell (blue), and their middle eigenvalues are listed in bold. The numerical values correspond to the composition $(Zr_{0.45}Hf_{0.55}O_2)_{0.775}(Y_{0.5}Nb_{0.5}O_2)_{0.225}$ having tetragonal lattice parameters $a_0 = 3.62263$ Å and $c_0 = 5.25509$ Å and monoclinic lattice parameters $a = 5.17640$ Å, $b = 5.18976$ Å, $c = 5.37569$ Å and $\theta = 98.58146°$. The general structure of the stretch matrices is similar for all compositions studied, but the numbers vary with composition.

which describe which atoms go where on transformation. This has been noticed by Hayakawa et al.[23,24] for the tetragonal-to-monoclinic transformation in $ZrO_2Y_2O_3$ and was confirmed by Pang et al.[11] in the ZrO_2CeO_2 system. We were alerted to this possibility here by running the StrucTrans algorithm[25]. For the correspondences with the smallest and next smallest strain, the algorithm yields essentially the two correspondences found by Hayakawa et al. and Pang et al. for our compositions. The only difference is that the algorithm gives two subcases for correspondence 1, labelled 1a and 1b in Figure 1. These correspond to switching the monoclinic *a* and *c* axes; however, they are not symmetry related.

Following measurements of lattice parameters on a limited set of compositions, we found that the compatibility between phases involving correspondence 2 could be significantly improved by increasing the Zr/Hf ratio. We did this, but rather than the expected lowering of hysteresis and improved reversibility, we observed exploding or weeping behaviour at the highest Zr/Hf ratio. The explosive behaviour on cooling through the transformation (Supplementary Video 1) typically resulted in the sample breaking into several pieces. Occasionally, specimens with a high Zr/Hf ratio jumped (Supplementary Video 2 and Extended Data Fig. 9), where the specimen is confined to a cylinder. Weeping is observed in Fig. 2a and in Supplementary Video 3. We confirmed by observations of the resulting powder in the scanning electron microscope that weeping corresponds to the gradual falling apart at the grain boundaries. On the other hand, consistent with work reported in ref. [8] (see also ref. [11]), our observations showed reversible behaviour and the lowest hysteresis in this system at the composition $y = 0.45$ where a condition

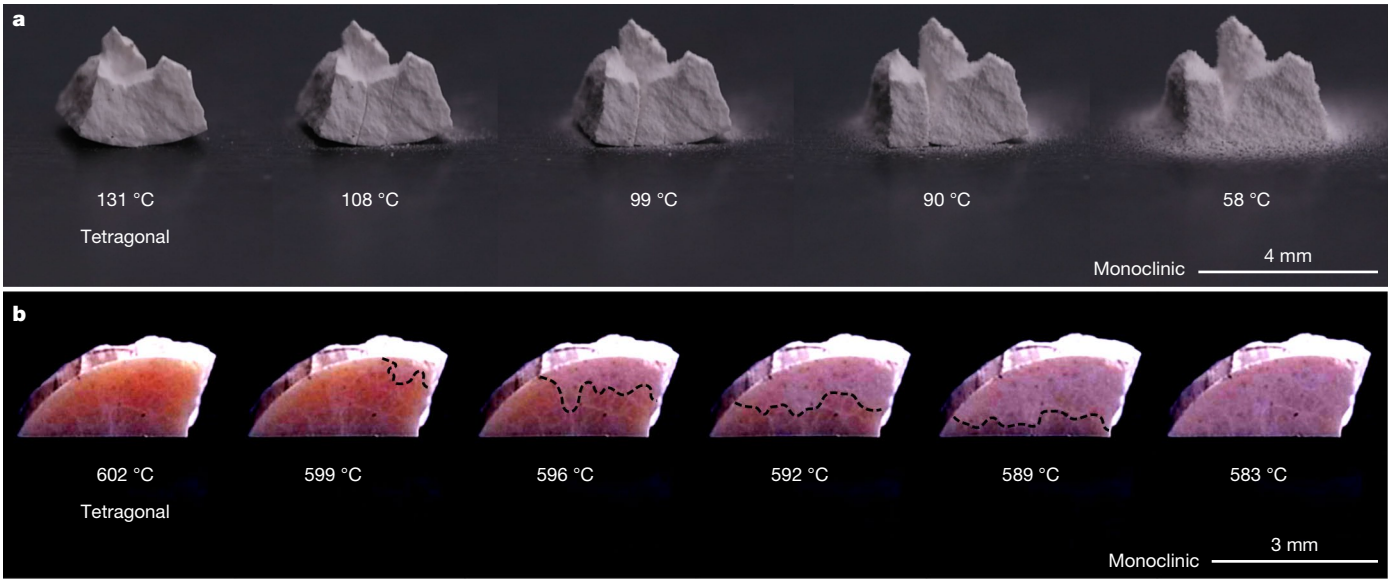

Fig. 2 | Frame sequences of martensitic transformation. a, Weeping on cooling in $(Zr_{0.9}Hf_{0.1}O_2)_{0.775}(Y_{0.5}Nb_{0.5}O_2)_{0.225}$. **b**, Reversible transformation in the composition $(Zr_{0.45}Hf_{0.55}O_2)_{0.775}(Y_{0.5}Nb_{0.5}O_2)_{0.225}$. The dashed line, added by hand, shows the approximate location of the interface. See Supplementary Videos 4 and 5 for additional clarity.

we term the equidistance condition is satisfied (Fig. 2b and Supplementary Videos 4 and 5).

These observations seem to contradict in several respects the accepted understanding of phase transformations. As a summary of the main points: the lowest hysteresis occurs at the equidistance condition, which has no known significance; tuning correspondence 2 to satisfy quite closely conditions of supercompatibility results in higher hysteresis, and weeping or explosion, rather than the expected reversible, lower hysteresis behaviour.

To understand these observations, we describe in more detail the analytical form of the conditions of compatibility. The transformation stretch matrix (Fig. 1) describes the linear transformation that maps the unit cell of the tetragonal lattice to that of the monoclinic lattice, and its middle eigenvalue is λ_2. The condition $\lambda_2 = 1$ is necessary and sufficient for a perfect unstressed interface between austenite and a single variant of martensite. The strongest conditions of supercompatibility are the cofactor conditions, which imply the existence of many simple and complex interfaces between phases with zero elastic energy. The equidistance condition is the statement $|\lambda_2^{(1a,b)} - 1| = |\lambda_2^{(2)} - 1|$, where the superscripts refer to the correspondence and λ_2 refers to the middle eigenvalue of the stretch matrix of that correspondence.

Figure 3a shows measured values (blue) of the width of the hysteresis loop $\Delta T = \frac{1}{2}(A_s + A_f - M_s - M_f)$ as a function of composition in $(Zr_yHf_{1-y}O_2)_{0.775}(Y_{0.5}Nb_{0.5}O_2)_{0.225}$. These temperatures define the onset and completion of the phase transformation: austenite start (A_s), austenite finish (A_f), martensite start (M_s), martensite finish (M_f). As seen from Fig. 3b, it is not possible by changing the Zr/Hf ratio to tune λ_2 for correspondence 1a,b to 1; it is simply too far away (Fig. 3b, uppermost curve). However, it is possible, by increasing the Zr/Hf ratio, to tune λ_2 of correspondence 2 to near 1 (Fig. 3b, lowermost curve). We did this and found $\lambda_2 = 0.99215$ at the highest Zr/Hf ratio of 100/0. However, rather than the expected lowering of hysteresis, we saw a rapid increase of hysteresis at these higher Zr/Hf ratios (Fig. 3a, blue) and the exploding or weeping behaviour.

We argue that this unusual behaviour originates from the two particular correspondences in this system, the polycrystal nature of the specimens and previously unrecognized conditions of compatibility that occur at equidistance. To investigate possible new conditions of compatibility under the equidistance condition, we report in the Supplementary Information a systematic analytical/numerical study, using measured lattice parameters for all compositions studied, of compatible interfaces between variants of the same correspondence, between variants of mixed correspondence and between all laminates of the same or mixed correspondence and the parent phase. As the equidistance condition involves both correspondences 1a,b and 2, our hypothesis was that the equidistance condition would imply new nongeneric compatible interfaces between variants of correspondences 1a,b and 2. Our theoretical study reported in the Supplementary Information shows that this is not the case.

We checked, as part of this study, the cofactor conditions. Recall that these conditions imply many planar and complex stress-free interfaces between phases. The cofactor conditions were not exactly satisfied for any composition. However, they could be considered approximately satisfied at certain compositions. From a physical viewpoint, approximate satisfaction of the cofactor conditions has the interpretation that the free energy of transition layers between the laminate and the parent can be made small. A suitable measure of this energy is the maximum value of a certain quadratic function $|q(f)|$ for values of f between 0 and 1 (Supplementary Section 2). Figure 3c shows this measure of satisfaction of the cofactor conditions plotted versus composition. This correlates quite closely with the equidistance condition.

To understand the paradoxical explosive behaviour when the middle eigenvalue of the stretch matrix for correspondence 2 is tuned to 1, we write explicitly the list of stretch matrices for the four variants of correspondence 2 in equation (1).

$$U_1 = \begin{bmatrix} \xi & \kappa & 0 \\ \kappa & \omega & 0 \\ 0 & 0 & \beta \end{bmatrix},\ U_2 = \begin{bmatrix} \omega & \kappa & 0 \\ \kappa & \xi & 0 \\ 0 & 0 & \beta \end{bmatrix},\ U_3 = \begin{bmatrix} \xi & -\kappa & 0 \\ -\kappa & \omega & 0 \\ 0 & 0 & \beta \end{bmatrix},\ U_4 = \begin{bmatrix} \omega & -\kappa & 0 \\ -\kappa & \xi & 0 \\ 0 & 0 & \beta \end{bmatrix} \quad (1)$$

Formulae for the normal strains $\xi - 1$, $\omega - 1$ and $\beta - 1$ and the shear strain κ are given in terms of the conventional lattice parameters a, b, c, θ, a_0 and c_0 in Supplementary Section 1, and illustrated geometrically in Fig. 1. Note that these four stretch matrices for correspondence 2 all

have the same determinant, and they have a common eigenvector (0,0,1) with the eigenvalue β. Complex microstructures are possible using just these four stretch matrices because rigid rotations are allowed and each pair of variants is compatible across two different twin planes, giving altogether 12 twin planes. Numerous laminated and more complex microstructures are possible, also involving the other correspondences (Supplementary Section 1). However, by tuning $\lambda_2^{(2)}$ to 1 we strongly favour transformation by correspondence 2.

Granted that correspondence 2 is favoured, we note that (on a connected domain) the necessary and sufficient conditions for a deformation to be a plane strain are that all stretch matrices satisfy the conditions: of having a common eigenvector/eigenvalue pair; and their determinants must be independent of the coordinate along that eigenvector[26]. This is true of the list in equation (1). In this case, the plane strain is a deformation in which every point must move in a plane perpendicular to the tetragonal *c* axis. Also, all points with the same *a*- and *b*-axis coordinates move with the same displacement. Despite numerous complex microstructures possible using just correspondence 2, they are all plane strains.

While plane strain deformations are easily possible in a single crystal, they are highly incompatible at a grain boundary separating grains of nonparallel *c* axes. The incompatibility is appreciated by considering a point on the grain boundary. To be consistent with a plane strain of both grains, it must move in two nonparallel planes. Thus, it must move along the straight line at their intersection. Unless the grain boundary is exceedingly special, this motion will take it off the grain boundary, an impossibility without grain boundary migration, which does not occur at the conditions studied.

In the region $y = 0.9$–1.0, both weeping and exploding were observed. No consistent compositional dependence of these behaviours could be seen. However, specimens with a shape having a near planar surface allowing for good thermal contact with the cooling plate exhibited the more violent macroscale fractures. In addition, specimens with a relatively large-area thermal contact are expected to have higher total heat flux, and the resulting large, approximately planar stressed transition layers provide larger energy release rates for transverse planar cracks, which have a tendency to produce explosive motion. A heat transfer analysis given in the Supplementary Section 3 supports these expectations.

While these conclusions are supported by our measurements, our work highlights the need for a general theory of compatibility that includes both phase boundaries and grain boundaries, and a full-atomic-resolution experimental study of grain boundaries in transforming ceramics.

In this Article, we have presented three disparate behaviours—exploding, weeping and reversible—demonstrated in the system $(Zr_yHf_{1-y}O_2)_{0.775}(Y_{0.5}Nb_{0.5}O_2)_{0.225}$. We show that the reversible behaviour is due to near satisfaction of strong conditions of compatibility (equidistance) that can be exploited in other cases. We also propose that cases of exploding and weeping originate from the particular structure of the variants of martensite of correspondence 2 that imply plane strain deformations. While these behaviours seem at first to contradict accepted principles, in fact they serve to widen the set of theory-driven tools applicable in the search for reversible transformations in ceramics. These include texturing and approximate satisfaction of the cofactor conditions. Our work also highlights the subtle interplay of multiple transformation correspondences. Taking our findings together, it is anticipated that these ideas will be important in the current worldwide search for a highly reversible shape-memory ceramic material.

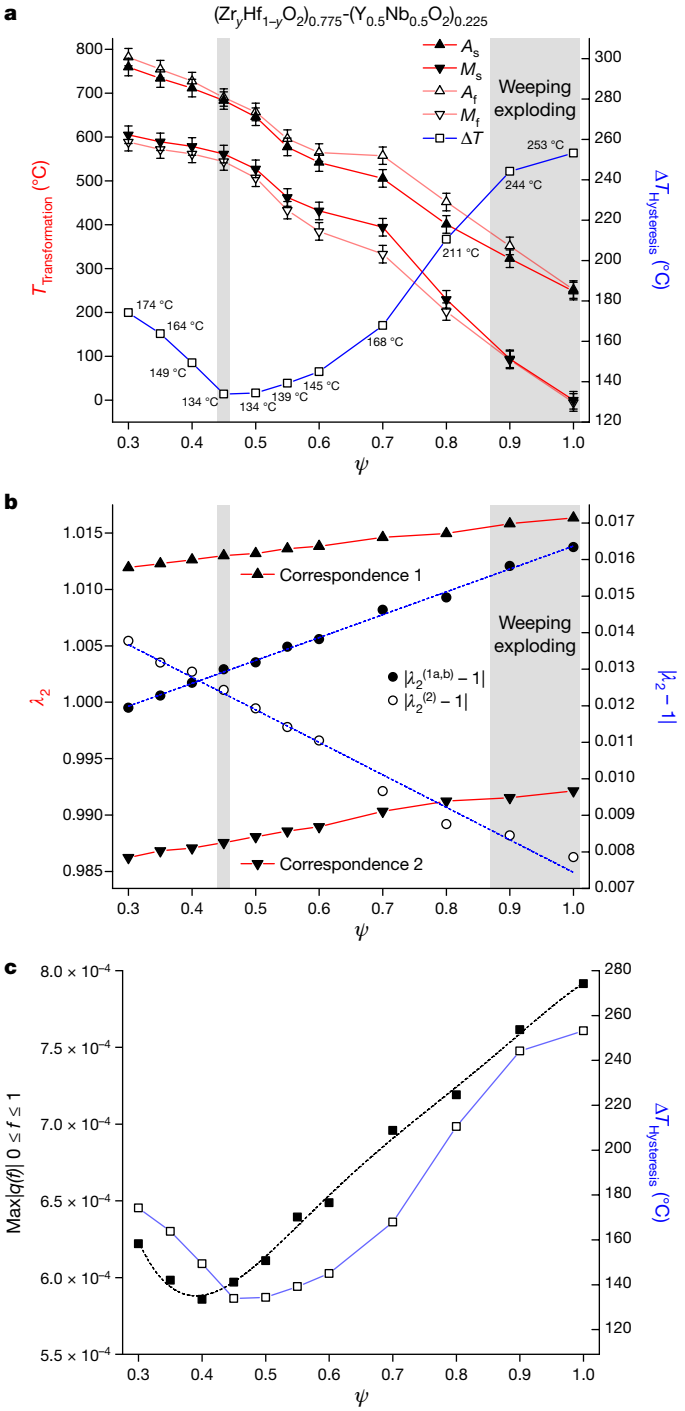

Fig. 3 | Thermal characterization and kinematic compatibility. **a**, Transformation temperatures and hysteresis $\frac{1}{2}(A_s + A_f - M_s - M_f)$. **b**, Values of λ_2. Note the lowest hysteresis in this system ($y = 0.45$) occurs where the equidistance condition $|\lambda_2^{(1a,b)} - 1| = |\lambda_2^{(2)} - 1|$ is satisfied (thin grey strip). **c**, Maximum deviation from satisfaction of the cofactor conditions based on measured lattice parameters. The condition $q(f) = 0$, together with an inequality that is satisfied in these cases, comprises the cofactor conditions.

Online content

Any methods, additional references, Nature Research reporting summaries, source data, extended data, supplementary information, acknowledgements, peer review information; details of author contributions and competing interests; and statements of data and code availability are available at https://doi.org/10.1038/s41586-021-03975-5.

1. Chen, X., Srivastava, V., Dabade, V. & James, R. D. Study of the cofactor conditions: conditions of supercompatibility between phases. *J. Mech. Phys. Solids* **61**, 2566–2587 (2013).

2. Chluba, C. et al. Ultralow-fatigue shape memory alloy films. *Science* **348**, 1004–1007 (2015).
3. Delville, R. et al. Transmission electron microscopy study of phase compatibility in low hysteresis shape memory alloys. *Philos. Mag.* **90**, 177–195 (2010).
4. Della Porta, F. On the cofactor conditions and further conditions of supercompatibility between phases. *J. Mech. Phys. Solids* **122**, 27–53 (2019).
5. Niitsu, K., Kimura, Y., Omori, T. & Kainuma, R. Cryogenic superelasticity with large elastocaloric effect. *NPG Asia Mater.* **10**, e457 (2018).
6. Zarnetta, R. et al. Identification of quaternary shape memory alloys with near-zero thermal hysteresis and unprecedented functional stability. *Adv. Funct. Mater.* **20**, 1917–1923 (2010).
7. Gu, H., Bumke, L., Chluba, C., Quandt, E. & James, R. D. Phase engineering and supercompatibility of shape memory alloys. *Mater. Today* **21**, 265–277 (2018).
8. Jetter, J. et al. Tuning crystallographic compatibility to enhance shape memory in ceramics. *Phys. Rev. Mater.* **3**, 93603 (2019).
9. Wegner, M., Gu, H., James, R. D. & Quandt, E. Correlation between phase compatibility and efficient energy conversion in Zr-doped barium titanate. *Sci. Rep.* **10**, 3496 (2020).
10. Liang, Y. G. et al. Tuning the hysteresis of a metal-insulator transition via lattice compatibility. *Nat. Commun.* **11**, 3539 (2020).
11. Pang, E. L., McCandler, C. A. & Schuh, C. A. Reduced cracking in polycrystalline ZrO_2-CeO_2 shape-memory ceramics by meeting the cofactor conditions. *Acta Mater.* **177**, 230–239 (2019).
12. Lai, A., Du, Z., Gan, C. L. & Schuh, C. A. Shape memory and superelastic ceramics at small scales. *Science* **341**, 1505–1508 (2013).
13. Kohn, R. V. & Müller, S. Branching of twins near an austenite—twinned-martensite interface. *Philos. Mag. A* **66**, 697–715 (1992).
14. Burkart, M. W. & Read, T. A. Diffusionless phase change in the indium-thallium system. *Trans. Am. Inst. Min. Metall. Eng.* **197**, 1516–1524 (1953).
15. Ball, J. M. & James, R. D. in *Analysis and Continuum Mechanics: a Collection of Papers Dedicated to J. Serrin on His Sixtieth Birthday* 647–686 (Springer, 1989).
16. Yang, S. et al. A jumping shape memory alloy under heat. *Sci. Rep.* **6**, 21754 (2016).
17. Yadava, K. et al. Extraordinary anisotropic thermal expansion in photosalient crystals. *IUCrJ* **7**, 83–89 (2020).
18. Naumov, P., Chizhik, S., Panda, M. K., Nath, N. K. & Boldyreva, E. Mechanically responsive molecular crystals. *Chem. Rev.* **115**, 12440–12490 (2015).
19. Tong, F. et al. Photomechanical molecular crystals and nanowire assemblies based on the [2+2] photodimerization of a phenylbutadiene derivative. *J. Mater. Chem. C* **8**, 5036–5044 (2020).
20. Chandrasekar, S. & Chaudhri, M. M. The explosive disintegration of Prince Rupert's drops. *Philos. Mag. B* **70**, 1195–1218 (1994).
21. Gibbs, J.W. *On the equilibrium of heterogeneous substances* Vol. 1 (Longmans Green and Co., 1879)
22. Chen, X. et al. Direct observation of chemical short-range order in a medium-entropy alloy. *Nature* **592**, 712–716 (2021).
23. Hayakawa, M., Kuntani, N. & Oka, M. Structural study on the tetragonal to monoclinic transformation in arc-melted ZrO_2-2mol.%Y_2O_3—I. Experimental observations. *Acta Metall.* **37**, 2223–2228 (1989).
24. Hayakawa, M. & Oka, M. Structural study on the tetragonal to monoclinic transformation in arc-melted ZrO_2-2mol.%Y_2O_3—II. Quantitative analysis. *Acta Metall.* **37**, 2229–2235 (1989).
25. Chen, X. & Song, Y. *Structural Phase Transformation Web Tools* (StrucTrans, 2014); http://www.structrans.org
26. Ball, J. M. & James, R. D. A characterization of plane strain. *Proc. Math. Phys. Sci.* **432**, 93–99 (1991).

Publisher's note Springer Nature remains neutral with regard to jurisdictional claims in published maps and institutional affiliations.

© The Author(s), under exclusive licence to Springer Nature Limited 2021

Methods

Sample fabrication

Ceramic samples in the $(Zr/Hf)O_2(YNb)O_4$ system were fabricated by the conventional solid-state route. $YNbO_4$ forms with ZrO_2 a substitutional solid solution, stabilizes the tetragonal zirconia phase to lower temperatures and therefore reduces the transformation temperatures. On the basis of the $(Zr_yHf_{1-y}O_2)_{0.775}(Y_{0.5}Nb_{0.5}O_2)_{0.225}$ system, we produced a series of compositions with y = 0.3, 0.35, 0.4, 0.45, 0.55, 0.6, 0.7, 0.8, 0.9 and 1.0.

The different raw powders of zirconium(IV) oxide (ZrO_2; calcined, 99%, ABCR), hafnium(IV) oxide (HfO_2; 99% (metal basis excluding Zr), Zr < 1.5%, ABCR), yttrium(III) oxide (Y_2O_3; 99.9% Y, ABCR) and niobium(V) oxide (Nb_2O_5; 99.99% trace metal basis, Sigma-Aldrich) were weighed and mixed to achieve the desired composition, followed by a grinding procedure in a planetary mill at 210 r.p.m. for 24 h. ZrO_2 balls served as grinding media and hexane as a lubricant, resulting in an average grain size < 50 nm.

The samples were subsequently calcined at 1,400 °C for 5 h to improve the density and compact strength. Adding polyvinyl alcohol as a binder required additional heating in the drying cabinet to 80 °C for several hours. Afterwards, milling by hand and sieving (125 µm mesh size) was performed to attain a deagglomeration of the powder particles. Using cold uniaxial pressing, 500 mg of the powder was compacted under 20 MPa load for 60 s into a pellet with a diameter of 6 mm and an approximate height of 5 mm. Without additional pressure, the green bodies were sintered in air in a two-step process. To eliminate residual carbon compounds, the green bodies were was pyrolysed at 500 °C for 8 h. The temperature was increased with a heating rate of 1 °C min^{-1}, followed by a temperature increase of 6 °C min^{-1} to 1,500 °C for 3 h, at which the sample was finally sintered.

Thermal analysis and error bars

The transition temperatures were determined by differential thermal analysis with a Netzsch STA 409 Cell (room temperature to 1,400 °C). To cover a larger temperature range, the thermal analysis was extended by the use of differential scanning calorimetry (DSC) measurements performed with a NETZSCH DSC 204 F1 Phoenix (−150 to 600 °C) differential scanning calorimeter. For all measured samples, the defined temperature profiles were controlled at a rate of 10 K min^{-1} during heating and cooling.

The transition temperatures are A_s, A_f, M_s, M_f for the austenite and martensite start and finish temperatures, respectively. Thermal hysteresis is calculated by the equation $\Delta T = ½(A_s + A_f - M_s - M_f)$. To obtain the transformation temperatures from the DTA or the DSC results, the method (intersection between the baseline–tangent and the tangent of the inflection point) was applied. DSC measurements were performed for samples with transformation temperatures below 600 °C, while DTA measurements were conducted for samples with y = 0.55 and lower. To ensure consistency between different samples and owing to a migration in transformation temperatures on repeated transformation, it is important to note that the measurements shown in this paper were taken from the first transformation cycle after sintering, with the exception of y = 1 owing to its stable tetragonal room-temperature phase. In the DSC measurements, a pan with a pierced lid was used; an empty one was taken as a reference material. In the DTA measurement, Al_2O_3 crucibles serve as containers. The reference material consisted of inert Al_2O_3 beads.

Owing to limited data, it was not possible to obtain meaningful statistical distributions to determine error bars in Fig. 3a. The error bars were therefore determined as follows: for measurements on a given sample, the maximum range of measured transformation temperatures of a given type (for example, $|\max A_s - \min A_s|$) was calculated. These ranges were then averaged over all measured samples, giving the length of the error bar (MR = ±19 K) as an estimated quantity, reflecting the mean range over all measurement results.

$$\mathrm{MR} = \frac{1}{N}\left(\frac{\sum_{y=0.3}^{1}|\max A_s - \min A_s| + \sum_{y=0.3}^{1}|\max A_f - \min A_f|}{4} + \frac{\sum_{y=0.3}^{1}|\max M_s - \min M_s| + \sum_{y=0.3}^{1}|\max M_f - \min M_f|}{4}\right) \quad (2)$$

Here y indicates the synthesized composition and N = 17 is the number of all measurements performed by thermal analysis.

Temperature-dependent X-ray diffraction measurements

General and temperature-dependent X-ray diffraction (XRD) measurements (Extended Data Figs. 7 and 8) were executed with a Rigaku SmartLab 9 kW system. The X-ray source generates Cu radiation with a wavelength of λ = 1.5406 Å. The system was operated at 45 kV and 200 mA with parallel beam optics and a two-dimensional array detector (HyPix-3000) on the receiving side running in one-dimensional mode. The XRD device is equipped with a domed heating stage (Anton Paar DHS1100) for in situ heating experiments. For temperatures below room temperature, a domed (Anton Paar DCS350) cooling stage was used.

In the high-temperature XRD experiments, a parallel beam geometry was chosen and $\theta/2\theta$ scans were performed in the range of 15° to 75°. The following measurement parameters were used: step width, 0.04°; scan speed, 4° min^{-1}; incident slit, 0.4 mm; receiving slit 1 and 2, 3.5 mm.

The XRD scans are used for determination of the lattice parameters in the monoclinic low-temperature and tetragonal high-temperature phase. To determine the different lattice parameters and the evolution of the molar phase fraction, we collect data at several temperatures. The heating and cooling to the intended temperature occurred at a rate of 20 K min^{-1} followed by a 30-s holding step before measurement.

Data analysis by Rietveld refinement

The Rietveld method was used for extraction of lattice parameters in the TOPAS v6 software by Alan Coelho. The Crystallographic Information File specifying the crystal structure was taken from the Crystallographic Open Database with modifications for monoclinic ZrO_2, tetragonal ZrO_2 and customizing the occupation probability at the Zr and Hf atomic coordinates. The tetragonal phase was refined in the $P4_2/nmc$ space group and the monoclinic phase was refined in the $P2_1/c$ space group. Gaussian and Lorentzian stress parameters were implemented for both crystal structures to correct the peak shape of the calculated diffraction curve. As we could identify a preferred (11-1) orientation of the monoclinic phase in the sintered sample caused by uniaxial pressing, this peak was considered during refinement.

Determination of transformation temperatures

The transition temperatures determined by DSC or DTA serve to set the temperature steps during in situ high-temperature XRD measurements, but transition temperatures deviate from those observed in the in situ experiments (up to 20 °C). The measured temperature of the thermocouple is taken below the hotplate of the stage and does not represent the real temperature of the interaction volume of the X-rays. Therefore, it is necessary to select an appropriate transformation temperature, which is used as a reference point for the λ_2 calculation of both lattice correspondences. In addition to the lattice parameter, the Rietveld method also yields the molar phase fraction for each phase. We used the fitting feature of the Origin 2017 software and defined an appropriate function $f(x) = \tanh(x)$ to trace the monoclinic phase fraction with temperature change. By detecting the inflection point of the twice differentiable function

$$f(x) = d_0 + d_1 + \tanh(d_2(-x + d_3))$$

we defined the transition temperature. This defines two transformation points per sample, one at the monoclinic-to-tetragonal transformation and another at the reverse transformation from the tetragonal to the monoclinic phase.

Possible rate effects

To check whether ordinary thermal stresses and relaxation or rate effects of the phase transformation played an important role, we saved a specimen that was part of a larger specimen whose martensite start temperature M_s was measured previously (3 times, for 3 separate pieces) to be between 0 and 5 °C. This specimen is in a high Zr compositional range where exploding/weeping are expected (wide grey-shaded region in Fig. 3). The saved specimen was held at approximately 21 °C for 94 days. We subjected this specimen to a cooling experiment seen in Supplementary Video 6. As can be seen from the video, this specimen jumped at 8 °C. This result further supports the assertion that neither ordinary thermal stresses nor rate effects are playing a prominent role. This result indicates that the stress that causes fracture is a direct result of the phase transformation.

Investigation of chemical homogeneity

The atomic-resolution transmission electron microscopy (TEM) studies reported in Extended Data Figs. 1–6 were carried out on a probe Cs-corrected Titan3 G2 60-300 microscope operating at 300 kV accelerating voltage and equipped with an extreme field emission gun high-brightness electron source. High-angle annular dark-field imaging was performed using an 80–200 mrad annular range for the high-angle annular dark-field detector. A probe-forming aperture of 20 mrad was used for imaging and for energy-dispersive X-ray (EDX) analysis. EDX maps were acquired with an FEI Super-X EDX detector system. The beam currents were limited to about 150 pA during the EDX mapping. The preparation of the cross-sectional specimen for TEM investigations was performed by a combination of focused gallium (30 keV, 15 keV, 5 keV and 2 keV) using a Zeiss Auriga dual beam system.

Data availability

The raw data that support the findings of this study are available at https://archive.materialscloud.org with the identifierhttps://doi.org/10.24435/materialscloud:6c-hk.

Acknowledgements R.D.J. and H.G. were supported by the NSF (DMREF-1629026), the MURI programme (FA9550-18-1-0095 and FA9550-16-1-0566) and a Vannevar Bush Faculty Fellowship. R.D.J. also acknowledges a Mercator Fellowship for the support of this German–US collaboration. E.Q., J.R. and J.J. acknowledge funding by the Deutsche Forschungsgemeinschaft (DFG) through a Reinhart Koselleck Project (313454214), and the project "Search for compatible zirconium oxide-based shape memory ceramics" (453203767). We thank N. Wolff for preliminary TEM measurements, and A. Mill for her assistance in the preparation of specimens for TEM investigation.

Author contributions H.G. and J.R. contributed equally to the manuscript. J.R. synthesized and characterized the samples. E.Q., J.R. and J.J. designed the compositions and J.J. also aided in characterization. L.K. and A.L. contributed to our understanding of the chemical homogeneity in this system. H.G. and R.D.J. developed the theory of compatibility and identified the significance of the equidistance condition with input from all authors. R.D.J. wrote the manuscript with input from all authors. E.Q. and R.D.J. supervised the collaboration.

Competing interests The authors declare no competing interests.

Additional information
Supplementary information The online version contains supplementary material available at https://doi.org/10.1038/s41586-021-03975-5.
Correspondence and requests for materials should be addressed to Hanlin Gu, Jascha Rohmer, Justin Jetter, Andriy Lotnyk, Lorenz Kienle, Eckhard Quandt or Richard D. James.
Peer review information *Nature* thanks Jian Luo and the other, anonymous, reviewer(s) for their contribution to the peer review of this work.
Reprints and permissions information is available at http://www.nature.com/reprints.

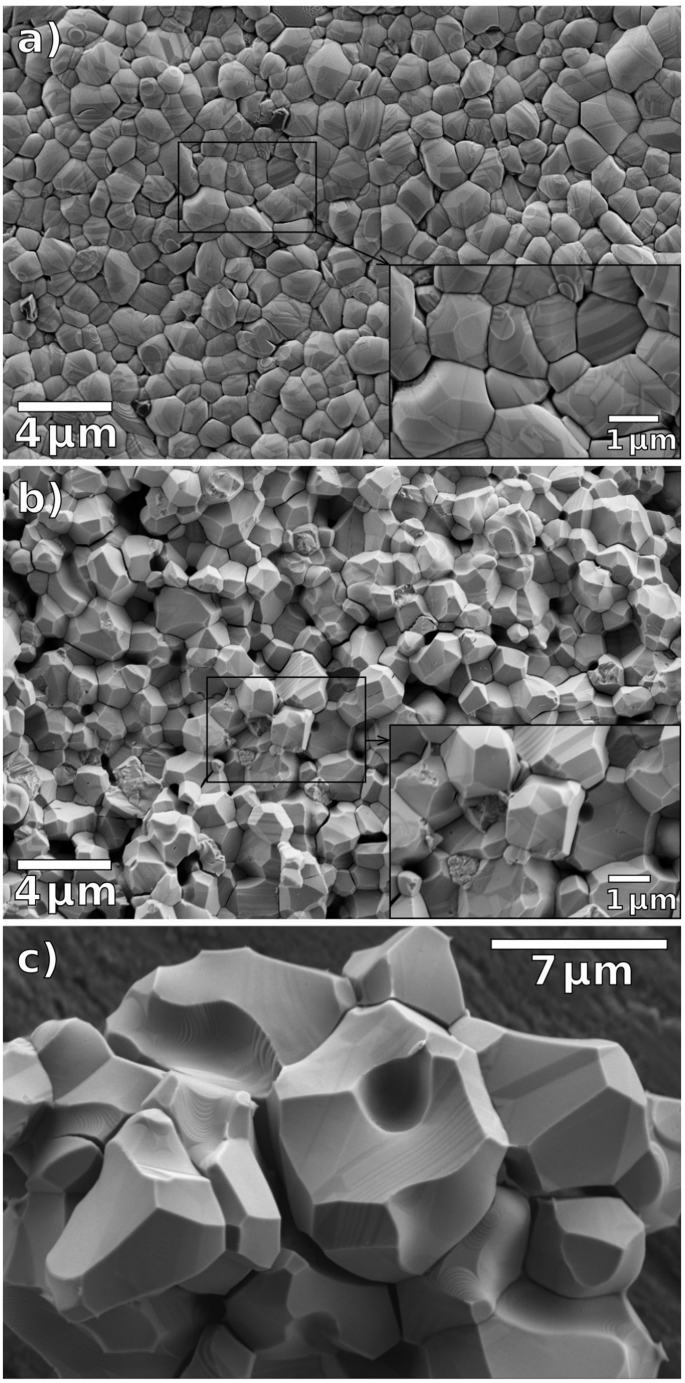

Extended Data Fig. 1 | Microstructure and grain size. (a) SEM image of the sample $y = 0.5$ with monoclinic twin laminated microstructure, showing the untreated sample surface directly after sintering, and (b) the fractured surface of the same sample. (c) Typical transformed material from a weeping sample that shows separation at the grain boundaries.

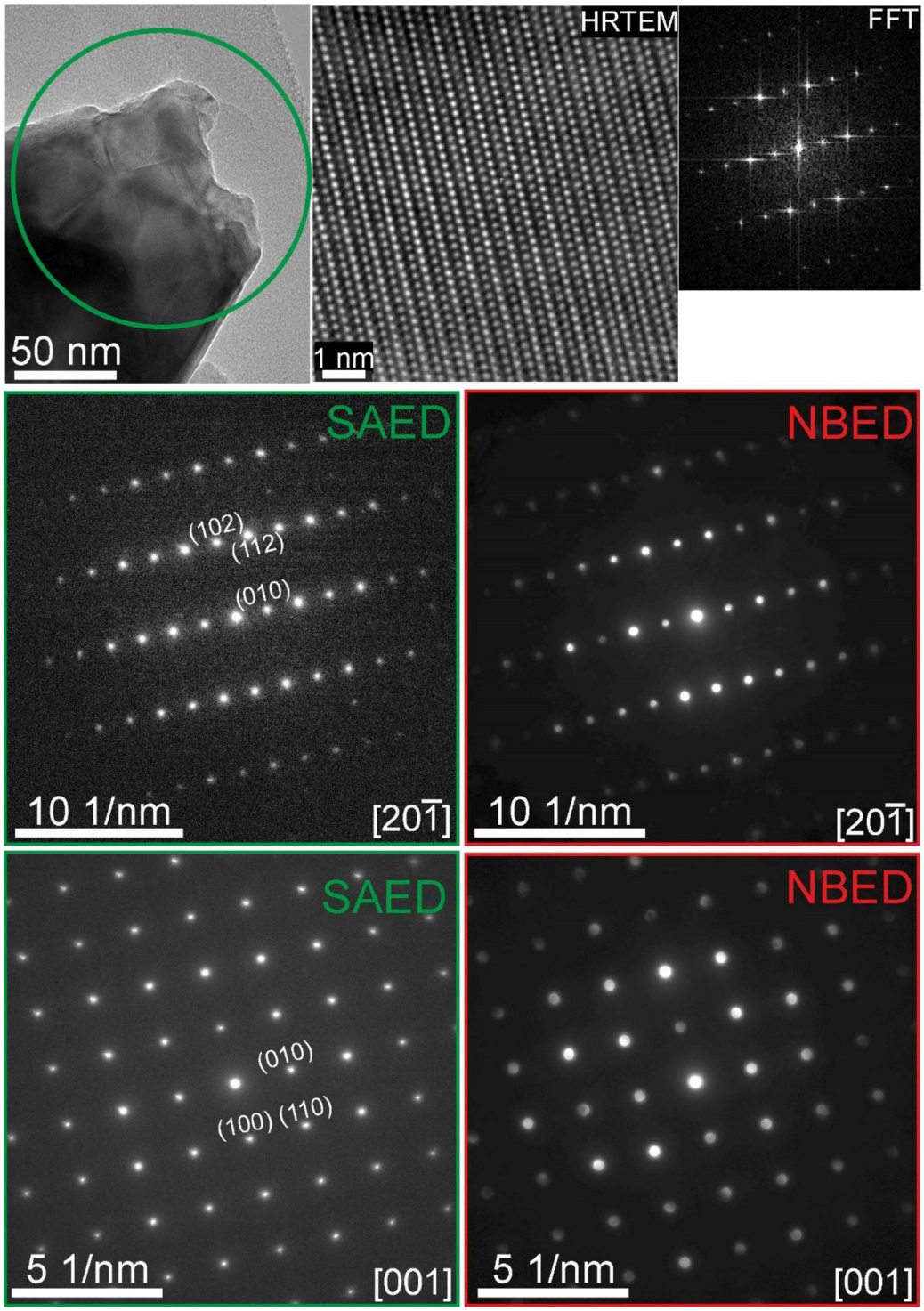

Extended Data Fig. 2 | Chemical homogeneity and absence of short-range ordering (crushed). The micrographs of the microstructural and nanoscale investigations are TEM and HRTEM images as well as SAED and NBED patterns of the $(Zr_{0.9}Hf_{0.1}O_2)_{0.775}(Y_{0.5}Nb_{0.5}O_2)_{0.225}$ (weeping) sample prepared by crushing. No additional reflections are observed in SAED and NBED patterns beyond those due to dynamical double diffraction. Also no additional reflections are seen in the FFT images.

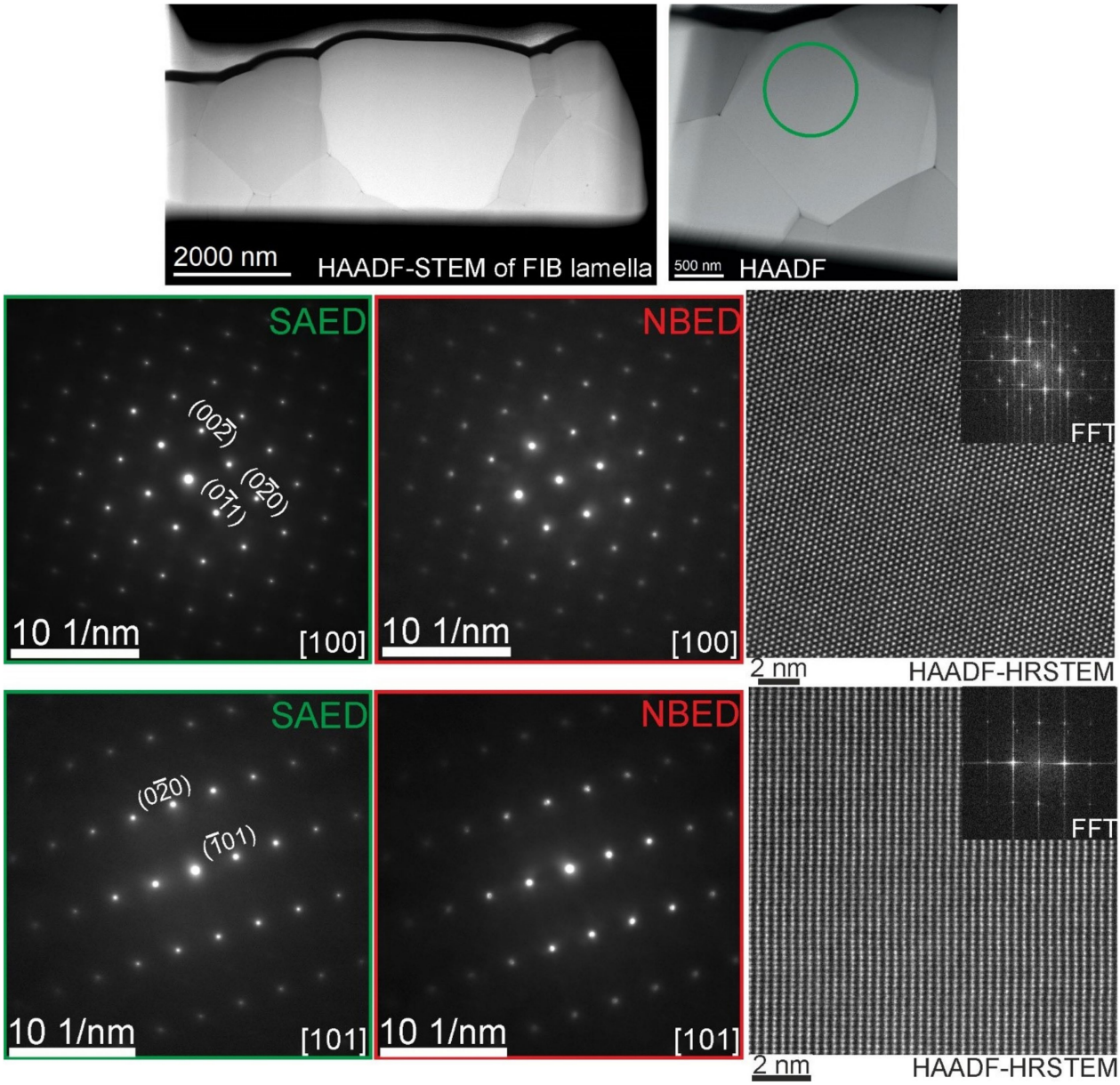

Extended Data Fig. 3 | Chemical homogeneity and absence of short-range ordering (FIB). The micrographs of the microstructural and nanoscale analysis are HAADF-STEM and HAADF-HRSTEM images as well as SAED and NBED patterns of the $(Zr_{0.9}Hf_{0.1}O_2)_{0.775}(Y_{0.5}Nb_{0.5}O_2)_{0.225}$ (weeping) sample, prepared by FIB. No additional reflections are observed in SAED, NBED patterns (only from dynamical double diffraction) as well as FFT images. Low-magnification HAADFM and atomic-scale HAADF micrographs are raw images, showing no significant intensity variation.

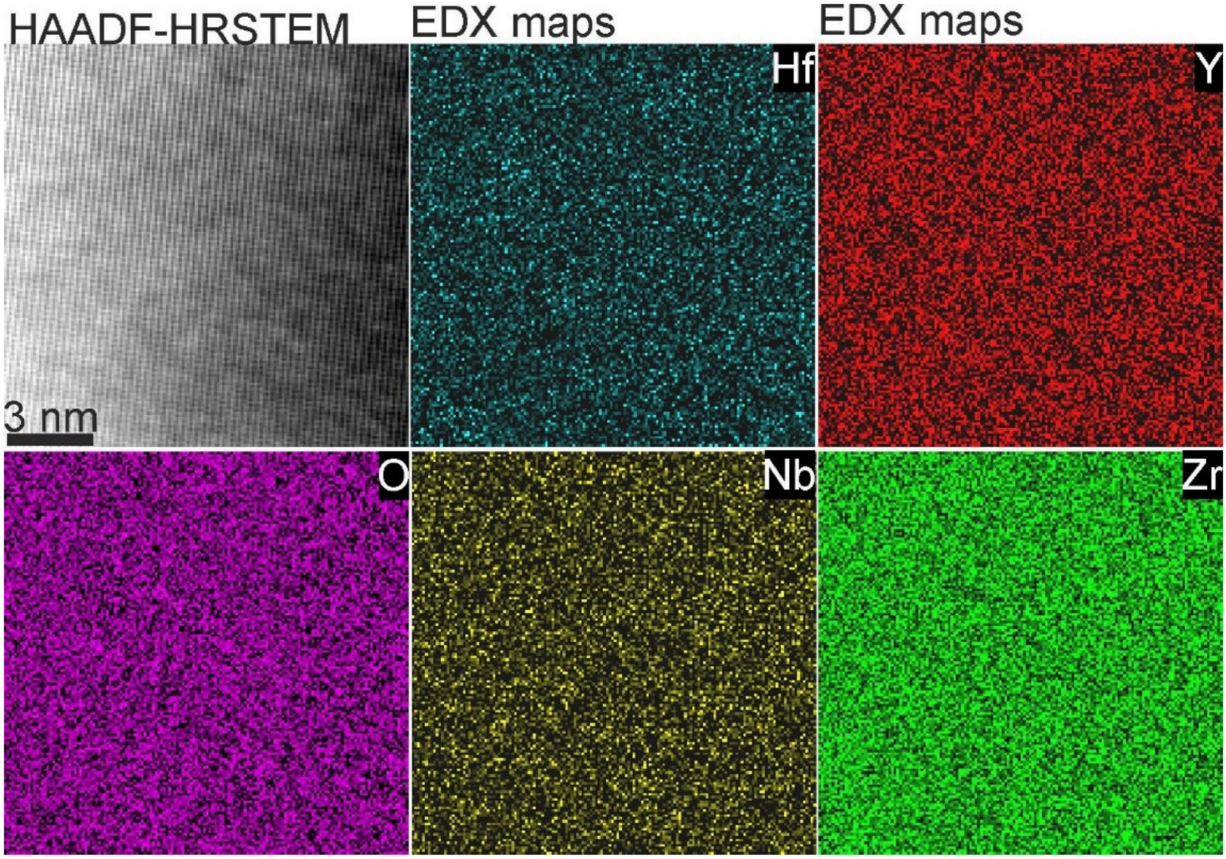

Extended Data Fig. 4 | Chemical homogeneity, crushed sample. Nanoscale chemical study of a $(Zr_{0.9}Hf_{0.1}O_2)_{0.775}(Y_{0.5}Nb_{0.5}O_2)_{0.225}$ (weeping) sample, prepared by crushing. The images are HAADF-HRSTEM micrograph and high resolution EDX elemental maps, suggesting a uniform distribution of elements.

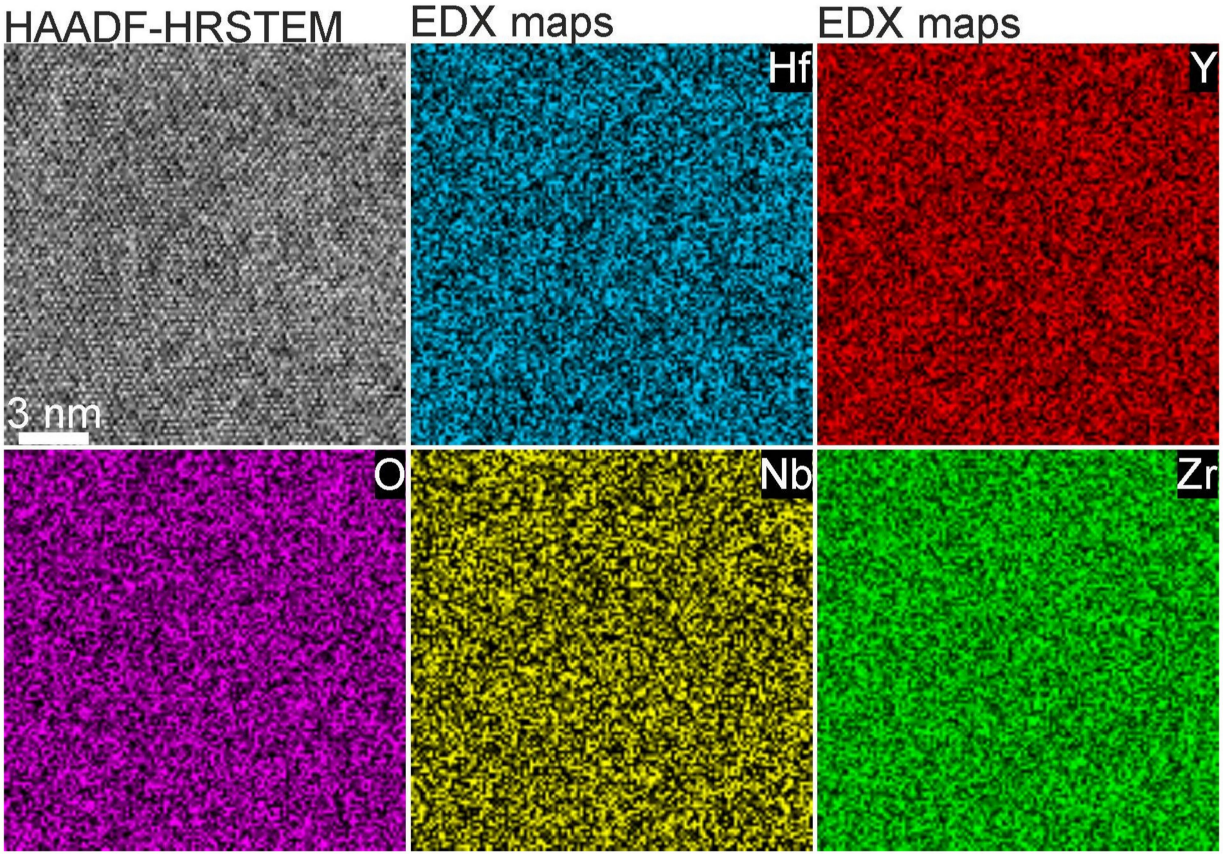

Extended Data Fig. 5 | Chemical homogeneity, FIB sample. Nanoscale chemical analysis of a $(Zr_{0.9}Hf_{0.1}O_2)_{0.775}(Y_{0.5}Nb_{0.5}O_2)_{0.225}$ (weeping) sample prepared by FIB. The images are HAADF-HRSTEM micrograph and high resolution EDX elemental maps, suggesting a uniform distribution of elements.

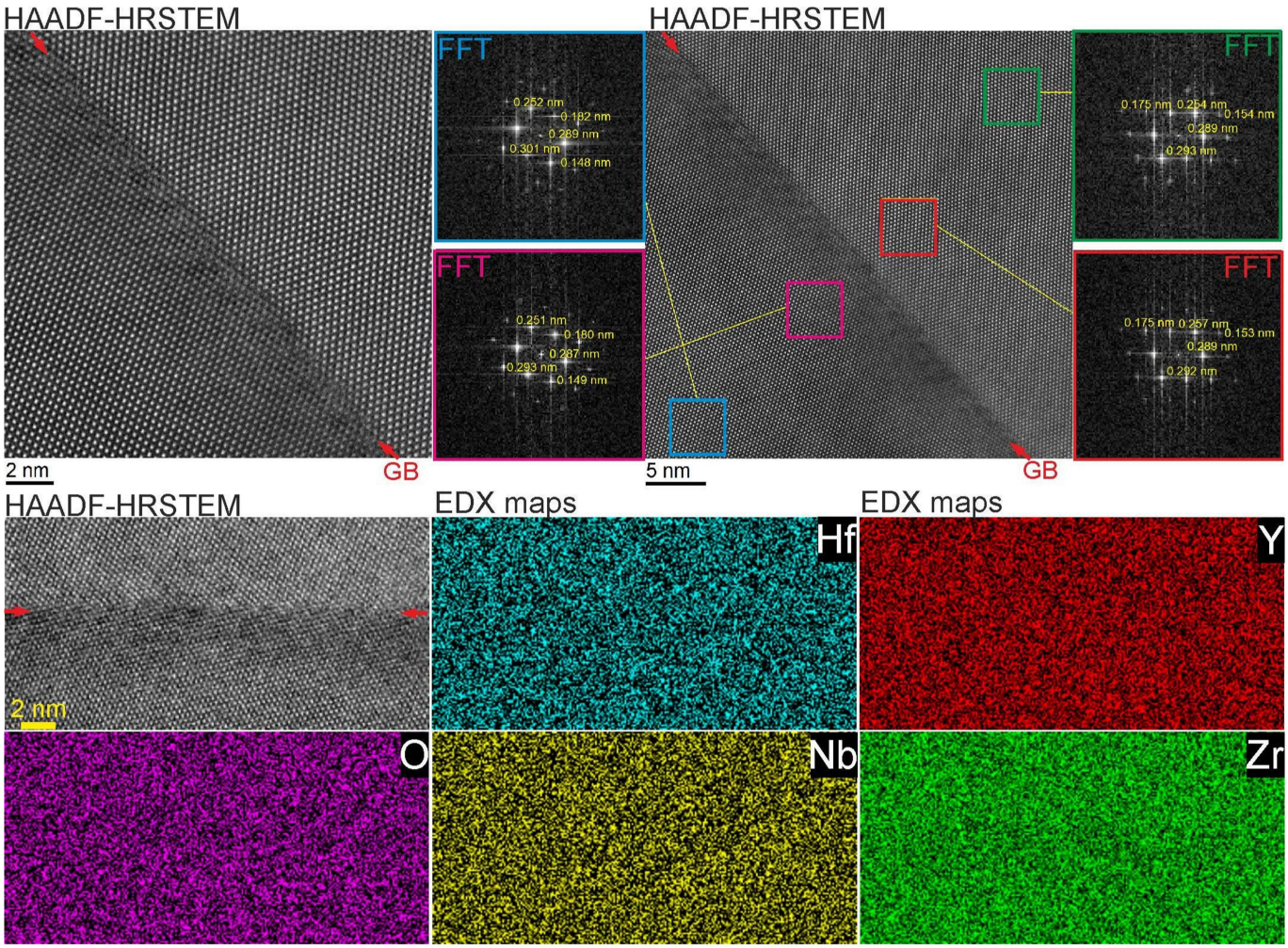

Extended Data Fig. 6 | Chemical homogeneity and structure at grain boundaries (FIB). Nanoscale study and local chemical analysis of a grain boundary of a $(Zr_{0.9}Hf_{0.1}O_2)_{0.775}(Y_{0.5}Nb_{0.5}O_2)_{0.225}$ (weeping) sample prepared by FIB. The micrographs are HAADF-STEM and HAADF-HRSTEM images as well as high resolution EDX elemental maps of the sample. Atomic-resolution HAADF micrographs are raw images, showing no significant intensity variation along the grain boundary (GB). The high resolution EDX maps suggest no significant element segregation at the grain boundary.

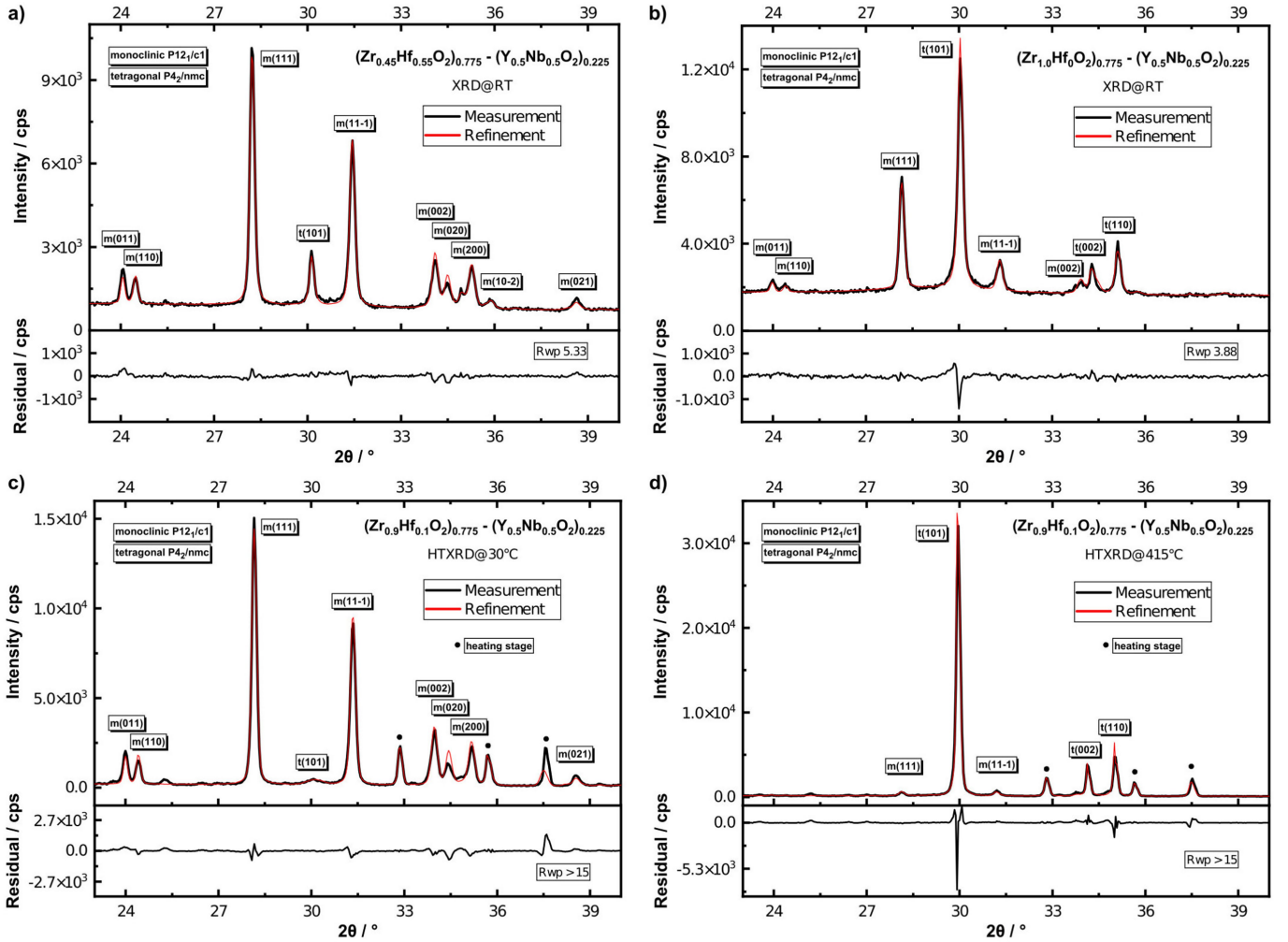

Extended Data Fig. 7 | Structure by X-Ray Diffraction with Rietveld Refinement. XRD diffraction pattern and calculated fit after Rietveld refinement (Top) with Topas software. The diagram at the bottom (Residual) shows the difference in intensity between the measured and calculated diffraction pattern. The sample in plot a) has a phase transformation above room temperature (RT) and is in the monoclinic phase, whereas the phase transformation of the sample in plot b) is below RT, so the pattern shows the tetragonal crystal structure. The low Rwp values, representing the goodness of the fit, indicate the quality of the Rietveld refinement. Temperature dependent measurements were conducted with a graphite domed heating stage. In c) the sample $y = 0.9$ is in its monoclinic phase, while in d) the measurement was taken at 415 °C following the monoclinic to tetragonal phase transition. The stage appears in the measured XRD pattern with additional peaks that were identified and excluded from the refinement done on the parameters of the physical phases. The resulting higher Rwp values compared to a) and b) can be explained by the reduced intensities due to limited transmissibility of the graphite dome used in these cases. Each measurement is refined up to 1000 times with different varied starting parameters with only the best fit being used for further calculations.

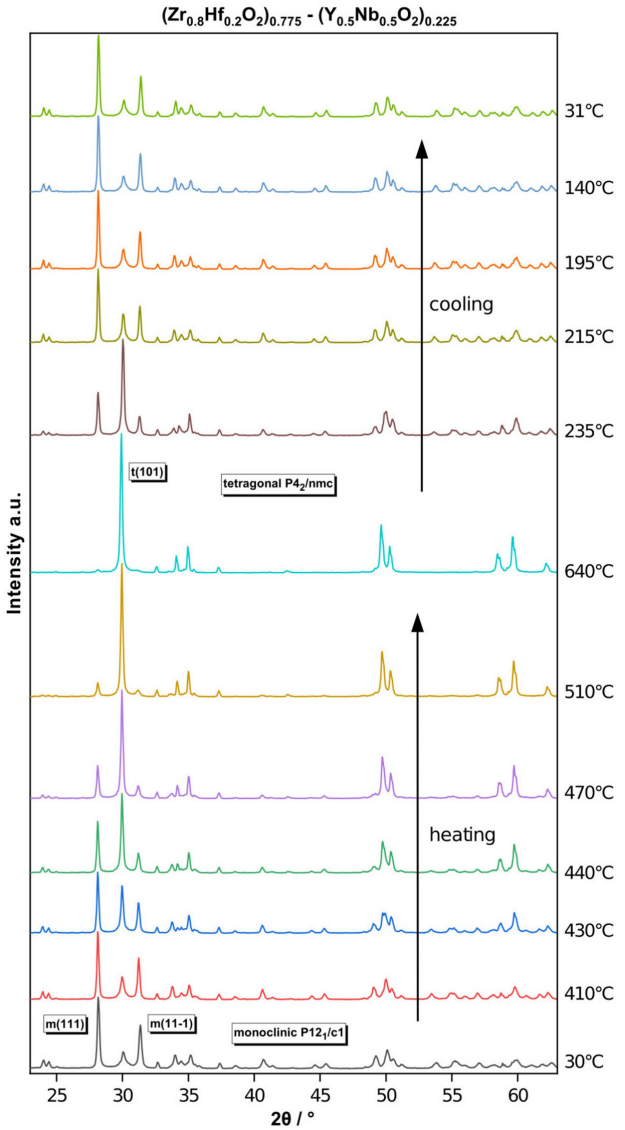

Extended Data Fig. 8 | Temperature dependent XRD measurements. Temperature dependent XRD measurement of the sample $y = 0.8$ with domed heating stage showing the phase transformation on heating and cooling. Upon heating, the characteristic tetragonal peak starts to grow at the austenitic start temperature and the monoclinic peaks are vanishing. At temperatures far above A_f we force transformation of the residual phase. During cooling to 30 °C, we observe the reverse transformation (t-to-m) of the sample. These measurements are the basis to obtain the lattice parameter of the monoclinic and tetragonal phases by Rietveld refinement, to determine the temperature dependent change of these lattice parameters and to calculate the middle eigenvalues λ_2 of the transformation stretch matrix for the lattice Correspondences 1_a, 1_b and 2.

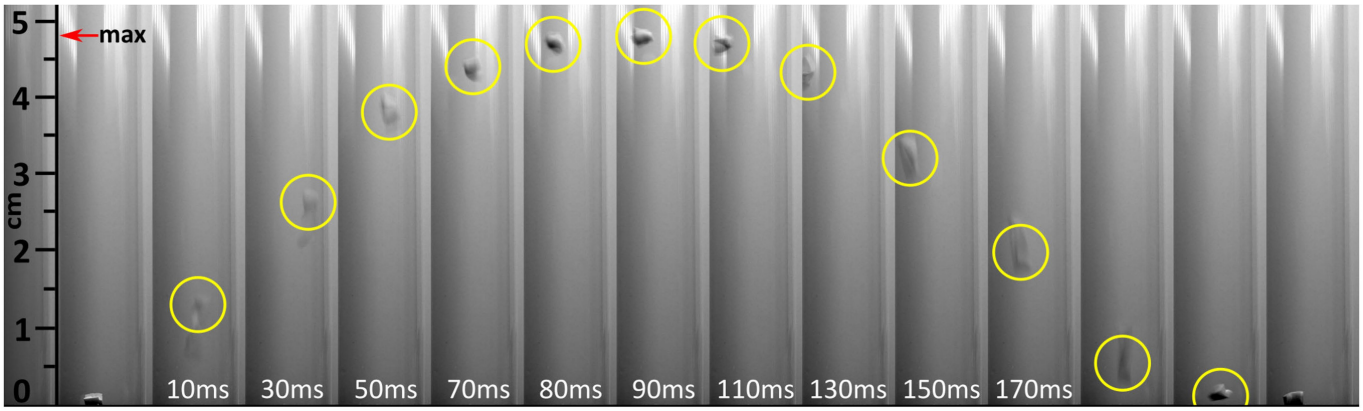

Extended Data Fig. 9 | Frame sequence of explosive behaviour. In a sequence of frames, the Fig. shows the path of a jumping ceramic confined to a cylinder. This jump is also shown in Supplementary Video 2.